RESEARCH ARTICLE | OCTOBER 25 2024

Wetting phenomena of droplets and gas bubbles: Contact angle hysteresis based on varying liquid–solid and solid–gas interfacial tensions

Franziska Aurbach ; Fei Wang ; Britta Nestler

J. Chem. Phys. 161, 164708 (2024)
https://doi.org/10.1063/5.0233997

The Journal of Chemical Physics ARTICLE pubs.aip.org/aip/jcp

Wetting phenomena of droplets and gas bubbles: Contact angle hysteresis based on varying liquid–solid and solid–gas interfacial tensions

Cite as: J. Chem. Phys. 161, 164708 (2024); doi: 10.1063/5.0233997
Submitted: 19 August 2024 • Accepted: 29 September 2024 •
Published Online: 25 October 2024

Franziska Aurbach,[1,2] Fei Wang,[1,2,a)] and Britta Nestler[1,2,3]

AFFILIATIONS

[1] Institute of Applied Materials-Microstructure Modelling and Simulation, Karlsruhe Institute of Technology, Straße am Forum 7, 76131 Karlsruhe, Germany
[2] Institute of Nanotechnology, Karlsruhe Institute of Technology, Hermann-von-Helmholtz-Platz 1, 76344 Eggenstein-Leopoldshafen, Germany
[3] Institute of Digital Materials Science, Karlsruhe University of Applied Sciences, Moltkestraße 30, 76133 Karlsruhe, Germany

[a)] **Author to whom correspondence should be addressed:** fei.wang@kit.edu

ABSTRACT

Wetting phenomena have been widely observed in our daily lives, such as dew on lotus leaf, and applied in technical applications, e.g., ink-jet printing. In contrast to constant liquid–solid and solid–gas interfacial tensions in Young's law, we here focus on the wetting phenomena by considering varying fluid–solid interfacial tensions. We analyze the energy landscape, the map of Young's contact angle, the number and corresponding contact angle of local energy minima, and the contact angle hysteresis for a liquid droplet on a solid substrate in a gas phase. In addition, a gas bubble on a solid substrate in a liquid phase has been scrutinized from the aspect of surface energy minimization. The wetting effect has been regarded, where the liquid and gas species penetrate into the solid phase on the microscopic scale [F. Wang and B. Nestler, Phys. Rev. Lett. **132**, 126202 (2024)]. We assume the liquid–solid and the solid–gas interfacial tensions to be a function dependent on the volume fraction of the liquid and the gas species and investigate the impact of the size ratio of the droplet to the solid surface that is overlooked in existing theories on the wetting phenomena. Our finding sheds light on the microscopic origin of the contact angle hysteresis and the droplet size effect on the wetting phenomena.

I. INTRODUCTION

A droplet depositing on a solid substrate in a gas phase, e.g., air, forms an apparent contact angle θ at the equilibrium, as shown in Fig. 1(b). This occurs, for example, with dew on leaves or with inkjet printing.[1,2] In Fig. 1, the liquid, gas, and solid phases are represented by L, G, and S, respectively. The interfacial tensions of liquid–gas, solid–liquid, and solid–gas are depicted by σ, $\gamma(\phi_L)$, and $\gamma(\phi_G)$, respectively. As considered in Ref. 3, we focus on a physical scenario that the liquid and the gas species penetrate into the solid phase with a depth of ℓ at the microscopic scale. This physical scenario is shown in Fig. 1(a). In the following, ϕ_L and ϕ_G stand for the compositions of the liquid species at the liquid–solid and liquid–gas interfaces, respectively. The equilibrium values of ϕ_L and ϕ_G are obtained by minimizing the total free energy of the system. We will also discuss the case of a gas bubble in a liquid phase on a solid substrate, for example, a gas bubble on a ship under water, as shown in Fig. 2, under conditions analogous to those for the liquid droplet.

In the case of Bond number much less than unity, which is the consideration of this work, the droplet forms a spherical cap. The formula of the spherical cap truncated by the solid substrate was derived in Appendix A,

$$V = \frac{\pi R^3}{3}(1-\cos\theta)^2(2+\cos\theta), \tag{1}$$

$$R = \left[\frac{3V}{\pi(1-\cos\theta)^2(2+\cos\theta)}\right]^{\frac{1}{3}}. \tag{2}$$

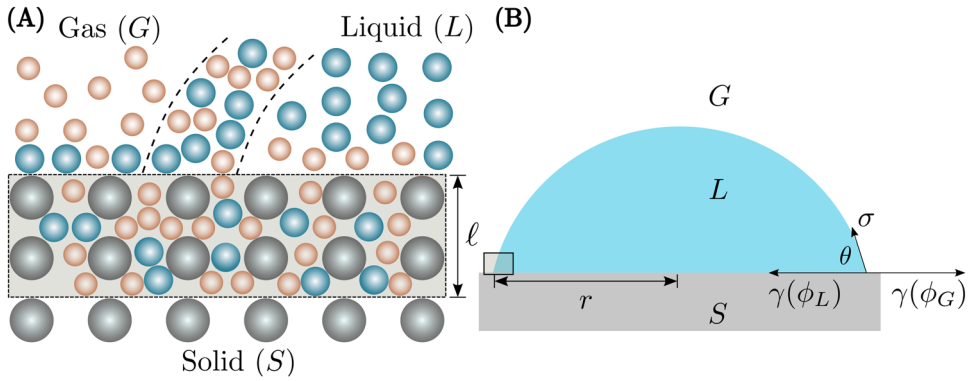

FIG. 1. (a) Sketch of the surface composition concept with a liquid droplet (*L*, blue) on a solid substrate (*S*, gray) in a gas phase (*G*, pink) with phases penetrating into each other. (b) Schematic cross-sectional view at the liquid droplet (*L*, blue) on a solid substrate (*S*, gray) in a gas phase (*G*, white) with the contact angle θ, the base radius r, and the interfacial tensions σ, $\gamma(\phi_L)$, and $\gamma(\phi_G)$.

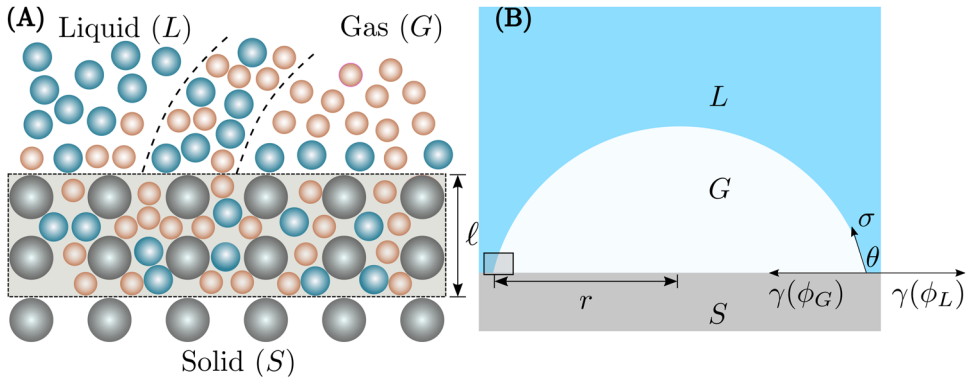

FIG. 2. (a) Sketch of the surface composition concept with a gas bubble (*G*, pink) on a solid substrate (*S*, gray) in a liquid phase (*L*, blue) with phases penetrating into each other. (b) Schematic cross-sectional view at the gas bubble (*G*, white) on a solid substrate (*S*, gray) in a gas phase (*L*, blue) with the contact angle θ, the base radius r, and the interfacial tensions σ, $\gamma(\phi_L)$, and $\gamma(\phi_G)$.

The formula for the surface area of the liquid–air interface S_d is derived in Appendix B, reading

$$S_d = 2\pi R^2(1-\cos\theta), \tag{3}$$

where R represents the cap radius, as shown in Fig. 3. The cap radius R is related to the base radius r as $r = R\sin\theta$. By assuming a flat homogeneous solid surface, as Thomas Young's work,[4] we express the total surface energy of the system as

$$E = \sigma S_d + \pi(R\sin\theta)^2\gamma_L + [S - \pi(R\sin\theta)^2]\gamma_G, \tag{4}$$

where S is the total surface area of the solid surface. The first term in Eq. (4) represents liquid–gas surface energy. The second term in Eq. (4) stands for the liquid–solid interfacial energy for a base area of πr^2. The last term in Eq. (4) denotes the solid–gas surface energy. It is noteworthy that the solid–liquid and solid–gas interfacial energies, γ_L and γ_G, are hard to be measured by experiments. In most previous studies, it is assumed that γ_G and γ_L are *constant*, and therefore, the term $S\gamma_G$ is neglected for deriving the equilibrium contact angles. By considering the volume constraint and defining $a = \gamma_G - \gamma_L$, we reformulate the total surface free energy as

$$E = \left[\frac{9\pi V^2}{(1-\cos\theta)(2+\cos\theta)^2}\right]^{\frac{1}{3}}[2\sigma - a(1+\cos\theta)].$$

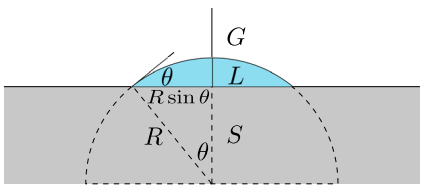

FIG. 3. Visualization of the base radius $r = R\sin\theta$ of the liquid droplet (L), which is represented by the blue area, in a gas phase (*G*, white) with the contact angle θ on the solid substrate (*S*, gray area).

The differentiation of E with respect to θ leads to

$$\frac{dE}{d\theta} = \left[\frac{9V^2\pi}{(1-\cos\theta)^4(2+\cos\theta)^5}\right]^{\frac{1}{3}} 2(a-\sigma\cos\theta)\sin\theta.$$

Solving the equation $dE/d\theta = 0$, we obtain the equilibrium contact angle θ, also known as Young's contact angle, as

$$\cos\theta = \frac{\gamma_G - \gamma_L}{\sigma}.$$

Hence, Young's law is derived.[1] Young's law can also be derived by the transversality condition according to the Bormashenko theory.[5] This derivation is valid for droplets with arbitrary sizes, although in the following, we focus on the cases with Bond number much less than unity.

In this work, we will consider that γ_G and γ_L depend on the compositions ϕ_L and ϕ_G, which denote the volume fractions of the liquid species penetrating into S at the solid–liquid and the solid–gas interface, respectively. When considering the interfacial tension γ_G and γ_L not to be constant, we use the same approach as in Ref. 3 for deriving the generalization of Young's law. We use $\gamma(\phi_L)$ and $\gamma(\phi_G)$ instead of constant values of γ_L and γ_G, with

$$\gamma(\phi) = \gamma_2\phi^2 + \gamma_1\phi + \gamma_0. \tag{5}$$

A similar parabolic formulation can be found in Ref. 6 within the context of diffuse interface based on Cahn's critical wetting theory.[7] The physical meaning of γ_2, γ_1, and γ_0 has been elucidated in Ref. 3. The coefficients γ_2, γ_1, and γ_0 are related to the difference of the internal energy Δp, internal energy of the gas phase p_G, penetration depth ℓ, van der Waals interaction χ of liquid–gas, the difference in the van der Waals force $\Delta\chi$ of liquid–solid and gas-solid χ_G as $\gamma(\phi) = \gamma_2\phi^2 + \gamma_1\phi + \gamma_0, \gamma_2 = -\ell\chi, \gamma_1 = \ell\chi\left(1 - \frac{\Delta p - \Delta\chi}{\chi}\right)$ and $\gamma_0 = \ell\chi\frac{p_G+\chi_G}{\chi}$. The total surface energy is analogous to the derivation of Young's equation and given by

$$E(\phi_L,\phi_G) = \sigma S_d + \pi(R\sin\theta)^2[\gamma(\phi_L) - \gamma(\phi_G)] + S\gamma(\phi_G). \tag{6}$$

The last term $S\gamma(\phi_G)$ was neglected in the literature[3] and in the next paragraph because of the assumption of constant solid–gas interfacial tension. In the current work, we will show that this term with varying solid–gas and solid–liquid interfacial tensions leads to new insights into the contact angle hysteresis and the droplet size effect.

By using Young's law, Eq. (6) can be transformed into the following equation:

$$\frac{E(\phi_L,\phi_G)}{\sigma(3V\sqrt{\pi})^{\frac{2}{3}}} = \left[2 + \frac{a(\phi_L,\phi_G)}{\sigma}\right]^{\frac{1}{3}}\left[1 - \frac{a(\phi_L,\phi_G)}{\sigma}\right]^{\frac{2}{3}}.$$

The equilibrium state is obtained by minimizing the total energy $\min\{E(\phi_L,\phi_G)|0 \le \phi_L \le 1, 0 \le \phi_G \le 1\}$. There are multiple local energy minima, leading to a generalized Young's law: $\cos\theta_{1,2} = \frac{\ell\chi}{4\sigma}\left(1 \pm \frac{\Delta p - \Delta\chi}{\chi}\right)^2$. It depends on the parameters, whether these minima are in the domain $\{(\phi_L,\phi_G)|0 \le \phi_L \le 1, 0 \le \phi_G \le 1\}$. A detailed discussion based on Wang and Nestler[3] follows later in this work.

In the present work, we will include the non-constant term $S\gamma(\phi_G)$ in the total free energy of the system Eq. (6), since $\gamma(\phi_G)$ is not a constant and but dependent of ϕ_G. With this new term, we will have alternative observations for the wetting phenomena comparing to the case where this term is neglected.[3]

In additional to the total free energy integration and minimization method for deriving Young's law, we note that there is another variational approach for deriving Young's law.[8–11] Within the context of diffuse interface, the liquid–gas interface has a finite width in the scale of nanometers; an order parameter ϕ is introduced to depict the local volume fraction of the liquid phase across the liquid–air interface. The wall free energy density is obtained by interpolating the liquid–solid and gas-solid interfacial energies as

$$f_w(\phi) = \gamma(\phi_G)h(\phi) + \gamma(\phi_L)[1 - h(\phi)]. \tag{7}$$

The interpolation function satisfies $h(\phi_G) = 1$ and $h(\phi_L) = 0$, so that we have $f_w(\phi_G) = \gamma(\phi_G)$ and $f_w(\phi_L) = \gamma(\phi_L)$. According to the variational approach, the natural boundary condition on S reads[7,12,13]

$$2\kappa\frac{d\phi}{dz} = \frac{df_w}{d\phi},$$

where κ is the gradient energy coefficient. By integrating the boundary condition from ϕ_L to ϕ_G across the liquid–gas interface near the solid wall, we obtain the following formulation:

$$\int_{\phi_L}^{\phi_G} 2\kappa\frac{d\phi}{dz}d\phi = \gamma(\phi_G) - \gamma(\phi_L).$$

With the geometrical relation, $\frac{d\phi}{dm}\cos\theta = \frac{d\phi}{dz}$ (see Fig. 1), as well as the definition of the liquid–gas interfacial tension according to Cahn,[7] $\sigma = \int_{\phi_L}^{\phi_G} 2\kappa\frac{d\phi}{dm}d\phi$, we can conclude

$$\begin{aligned}\int_{\phi_L}^{\phi_G} 2\kappa\frac{d\phi}{dz}d\phi &= \int_{\phi_L}^{\phi_G} 2\kappa\frac{d\phi}{dm}\cos\theta d\phi \\ &= \cos\theta\int_{\phi_L}^{\phi_G} 2\kappa\frac{d\phi}{dm}d\phi = \sigma\cos\theta,\end{aligned}$$

and therefore, the Young's law, $\sigma\cos\theta = \gamma(\phi_G) - \gamma(\phi_L)$ holds. It should be noted that the variational approach of Young's law is only suitable for continuous use. In the case of numerical implementation, one has to assume

$$\left.\frac{d\phi}{dz}\right|_L = \left.\frac{d\phi}{dz}\right|_S, \quad \text{or} \quad \left.\frac{d\phi}{dz}\right|_+ = \left.\frac{d\phi}{dz}\right|_-, \tag{8}$$

as shown in Fig. 4(b). Other extrapolation strategies have also been used in the literature[14] by introducing the so-called ghost cells. In the current work, we adopt the integration concept of Young's law by considering the minimization of the total surface energy. The benefit of the integration concept is its application to multiscale wetting phenomena, e.g., a microliter droplet on a solid surface with roughness in the order to nanometers.

The remaining manuscript is structured as follows: first, we consider a liquid droplet on a solid substrate in a gas phase in Secs. II and III. In Sec. II, we derive and analyze the energy formula with non-constant $\gamma(\phi_L)$ and $\gamma(\phi_G)$ and by including $S\gamma(\phi_G)$. Based on

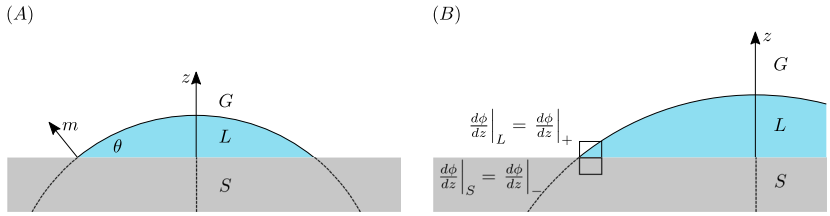

FIG. 4. Liquid droplet (*L*, blue) in a gas phase (*G*, white) on a solid substrate (*S*, gray) with (a) the illustration of the normal direction of the liquid–gas-interface *m* and the vertical direction *z* of the differential approach of Young's law for a liquid droplet (*L*, blue) in a gas phase (*G*, white) on a solid substrate (*S*, gray) and (b) the illustration of $\frac{d\phi}{dz}\big|_S$ and $\frac{d\phi}{dz}\big|_L$ of the differential approach of Young's law for numerical use.

this, the energy landscape, Young's contact angle map, and shapes of the droplet at the local energy minimum states are plotted, scrutinized, and compared for different values of γ_1 and $S/V^{\frac{2}{3}}$. In addition, we consider a gas bubble on a solid substrate in the liquid phase in Sec. IV and compare this result to the case of a liquid droplet on a solid substrate in a gas phase. This is followed by a comparison of the results ith the literature in Sec. V, a conclusion in Sec. VI, and an outlook in Sec. VII.

II. FREE SURFACE ENERGY OF A LIQUID DROPLET

In this section, we consider a liquid droplet in a gas phase on a solid substrate, as shown in Fig. 1. Figure 3 shows the base radius $r = R\sin\theta$ of the droplet. The half center angle of the spherical cap, marked by θ shown in Fig. 3, is equivalent to the apparent contact angle; see Appendix A.

We use $\gamma(\phi_L)$ and $\gamma(\phi_G)$ to describe the $L-S$ and $S-G$ surface tension, respectively. The parameters,

$$\phi_L = \frac{V_{LL}}{V_{LL}+V_{GL}} \tag{9}$$

and

$$\phi_G = \frac{V_{LG}}{V_{LG}+V_{GG}} \tag{10}$$

represent the volume fraction of the liquid species penetrating into *S* at the solid–liquid and the solid–gas interface, respectively. According to the definition, we have $0 \le \phi_L \le 1, 0 \le \phi_G \le 1$. The physical meanings of V_{LL}, V_{GL}, V_{LG}, and V_{GG} are as follows.

- V_{LL}: volume of liquid penetrating into the solid beneath the liquid droplet;
- V_{GL}: volume of gas penetrating into the solid beneath the liquid droplet;
- V_{LG}: volume of liquid penetrating into the solid under the gas phase; and
- V_{GG}: volume of gas penetrating into the solid under the gas phase.

We choose $\gamma(\phi)$ to be a quadratic function Eq. (5) of ϕ with $\gamma_2 = -\ell\chi$, $\gamma_1 = \ell\chi\left(1-\frac{\Delta p-\Delta\chi}{\chi}\right)$, and $\gamma_0 = \ell\chi\frac{p_G+\chi_G}{\chi}$. The value of p_G represents the internal energies of liquid and gas phases, and χ_G depicts the van der Waals interactions of liquid–solid and solid–gas. We define the pressure forces Δp due to the density asymmetry and the van der Waals forces $\Delta\chi$, which determine the wettability of the system with hydrophilicity when $\Delta\chi < 0$ and hydrophobicity when $\Delta\chi > 0$ Ref. 3. The Flory parameter χ characterizes the $L-G$ intermolecular potential. The penetration depth of fluids into the solid is described by ℓ.

For the sake of brevity and convenience, we introduce a function *a* as

$$a(\phi_L,\phi_G) = \gamma(\phi_G) - \gamma(\phi_L).$$

We assume the volume of the droplet *V* to be constant, e.g., no evaporation or condensation. The total surface energy consists of three contributions,

$$\begin{aligned} E(\phi_L,\phi_G) &= \sigma S_d + \pi(R\sin\theta)^2\gamma(\phi_L) + [S-\pi(R\sin\theta)^2]\gamma(\phi_G) \\ &= \sigma S_d - \pi(R\sin\theta)^2[\gamma(\phi_G)-\gamma(\phi_L)] + \gamma(\phi_G)S \\ &= \sigma S_d - \pi(R\sin\theta)^2 a(\phi_L,\phi_G) + \gamma(\phi_G)S. \end{aligned} \tag{11}$$

The first contribution comes from the liquid–gas cap energy. The second term is due to the contact of liquid with solid, forming a circular base area. The last term is engendered by the solid–gas interface.

For constant values of γ, the last term is constant and, therefore, omitted.[1] Due to the dependency of $\gamma(\phi)$ on ϕ, we include the additional term $\gamma(\phi_G)S$ in the following energy formula, which is the central consideration of this work. By substituting Eq. (3) into this equation and setting $g = \pi R^2$, we obtain

$$E(\phi_L,\phi_G) = g[2\sigma(1-\cos\theta) - (\sin\theta)^2 a(\phi_L,\phi_G)] + \gamma(\phi_G)S.$$

With Eq. (2), we can rewrite the total energy *E* as follows:

$$E(\phi_L,\phi_G) = \omega[2\sigma - 2\sigma\cos\theta - (\sin\theta)^2 a(\phi_L,\phi_G)] + \gamma(\phi_G)S, \tag{12}$$

with a non-zero factor $\omega = \left[\frac{9V^2\pi}{(1-\cos\theta)^4(2+\cos\theta)^5}\right]^{\frac{1}{3}}$. With the calculation in Appendix C, we can transform Eq. (12) into

$$E(\phi_L,\phi_G) = \Psi[2\sigma - a(\phi_L,\phi_G)(1+\cos\theta)] + \gamma(\phi_G)S, \tag{13}$$

with a factor $\Psi = \left[\frac{9V^2\pi}{(1-\cos\theta)(2+\cos\theta)^2}\right]^{\frac{1}{3}}$. The derivative $\frac{dE}{d\theta}$ was calculated in Appendix D,

$$\frac{dE(\phi_L,\phi_G)}{d\theta} = 2\omega[a(\phi_L,\phi_G) - \sigma\cos\theta]\sin\theta. \tag{14}$$

Therefore, we obtain Young's law as the solution of $\frac{dE(\phi_L,\phi_G)}{d\theta} = 0$ as

$$\cos\left(\theta(\phi_L,\phi_G)\right) = \frac{a(\phi_L,\phi_G)}{\sigma}. \tag{15}$$

It can be observed that Young's law does not depend on the additional term $\gamma(\phi_G)S$. Substituting Young's Eq. (15) into Eq. (13) and based on the calculations in Appendix E, we obtain the following equation:

$$\frac{E(\phi_L,\phi_G)}{\sigma(3V\sqrt{\pi})^{\frac{2}{3}}} = (2+\mu)^{\frac{1}{3}}(1-\mu)^{\frac{2}{3}} + \frac{\gamma(\phi_G)S}{\sigma(3V\sqrt{\pi})^{\frac{2}{3}}}, \tag{16}$$

with

$$\mu = \frac{a(\phi_L,\phi_G)}{\sigma}. \tag{17}$$

The equilibrium state of the system is obtained via the energy minimization,

$$\min\left\{E(\phi_L,\phi_G)|0 \le \phi_L \le 1, 0 \le \phi_G \le 1\right\}. \tag{18}$$

In following sections, we will show different plots of the energy landscape, the Young's contact angle, the number and corresponding contact angle of the local energy minima, and the contact angle hysteresis according to Eqs. (16) and (18).

A. Finding the critical points of the energy of the liquid droplet

Figure 5 shows the possible energy minima, marked by the green and blue crosses, and the possible saddle point or maximum, marked by the red cross, in the considered gray domain,

$$\Omega := \left\{(\phi_L,\phi_G)|0 \le \phi_L \le 1, 0 \le \phi_G \le 1\right\}. \tag{19}$$

These points and the existence of the critical points will be analyzed in this section.

We are looking for real values of local minima of $E(\phi_L,\phi_G)$ in Ω. At first, we set $\phi_L = 0$ or $\phi_L = 1$ and solve $\frac{dE(\phi_L,\phi_G)}{d\phi_G} = 0$ to address

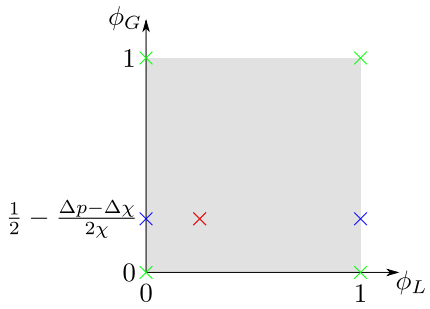

FIG. 5. Possible energy minima on $\{(\phi_L,\phi_G)|0 \le \phi_L \le 1, 0 \le \phi_G \le 1\}$ (gray domain) denoted by the green crosses [corners $(0,0)$, $(1,0)$, $(0,1)$ and $(1,1)$] and the blue crosses (with $\frac{dE(0,\phi_G)}{d\phi_G} = 0$ on the left and $\frac{dE(1,\phi_G)}{d\phi_G} = 0$ on the right) and possible saddle point or maximum at the red cross (with $\frac{dE(\phi_L,\phi_G)}{d\phi_G} = 0$ and $\frac{dE(\phi_L,\phi_G)}{d\phi_L} = 0$).

the equilibrium value of ϕ_G. With $\phi_L = 0$, we obtain $\phi_{G,0} = \frac{1}{2} - \frac{\Delta p - \Delta\chi}{2\chi}$ and the equilibrium contact angle,

$$\cos\theta = \frac{\gamma(\phi_{G,0}) - \gamma(0)}{\sigma} = \frac{\ell\chi}{4\sigma}\left(1 - \frac{\Delta p - \Delta\chi}{\chi}\right)^2.$$

This point is a local energy minimum, if $\phi_{G,0} = \frac{1}{2} - \frac{\Delta p - \Delta\chi}{2\chi} \in (0,1)$ or analogously $0 < \gamma_1 < \ell\chi$ and

$$\frac{d^2E(1,\phi_{G,0})}{d\phi_G^2} = \ell\chi\left[\frac{(144\pi V^2)^{\frac{1}{3}}(4\sigma\chi + b_0\ell)}{(8\sigma\chi + b_0\ell)^{\frac{2}{3}}(8\sigma\chi - 2b_0\ell)^{\frac{1}{3}}} - 2S\right] < 0,$$

with $b_0 = (\chi - \Delta\chi + \Delta p)^2$ holds. With $\phi_L = 1$, we get $\phi_{G,1} = \frac{1}{2} - \frac{\Delta p - \Delta\chi}{2\chi}$ and the equilibrium contact angle,

$$\cos\theta = \frac{\gamma(\phi_{G,1}) - \gamma(1)}{\sigma} = \frac{\ell\chi}{4\sigma}\left(1 + \frac{\Delta p - \Delta\chi}{\chi}\right)^2.$$

This point is a local energy minimum, if $\phi_{G,1} = \frac{1}{2} - \frac{\Delta p - \Delta\chi}{2\chi} \in (0,1)$ or analogously $0 < \gamma_1 < \ell\chi$ and

$$\frac{d^2E(0,\phi_{G,1})}{d\phi_G^2} = \ell\chi\left[\frac{(144\pi V^2)^{\frac{1}{3}}(4\chi\sigma + b_1\ell)}{(8\chi\sigma + b_1\ell)^{\frac{2}{3}}(8\chi\sigma - 2b_1\ell)^{\frac{1}{3}}} - 2S\right] < 0,$$

with $b_1 = (\chi - \Delta p + \Delta\chi)^2$ holds. These points are denoted by the blue crosses shown in Fig. 5. Due to the dependency of $\frac{d^2E(1,\frac{1}{2}-\frac{\Delta p-\Delta\chi}{2\chi})}{d\phi_G^2}$ or $\frac{d^2E(0,\frac{1}{2}-\frac{\Delta p-\Delta\chi}{2\chi})}{d\phi_G^2}$ on S, the existence of an energy minimum at $\left(0, \frac{1}{2} - \frac{\Delta p - \Delta\chi}{2\chi}\right)$ and $\left(1, \frac{1}{2} - \frac{\Delta p - \Delta\chi}{2\chi}\right)$ depends on S. The remaining solutions of $\frac{dE(\phi_L,\phi_G)}{d\phi_G} = 0$ are either complex for all values of S or complex for $S > 0$ and undefined for $S = 0$, since these solutions contain the term $\left(3\sqrt{\pi}\sqrt{\frac{1}{9\pi V^2 + S^3}}V - 1\right)^{-\frac{1}{3}}$. For physical meaning, we assume $S > 0$ and $V \ge 0$. We can follow $S \le 0$ from $3\sqrt{\pi}\sqrt{\frac{1}{9\pi V^2+S^3}}V - 1 \ge 0$. This leads to a contradiction to $S > 0$, and thus, the solutions are complex for $S > 0$. For $S = 0$, the term $\left(3\sqrt{\pi}\sqrt{\frac{1}{9\pi V^2+S^3}}V - 1\right)^{-\frac{1}{3}}$ and thus the solutions of $\frac{dE(\phi_L,\phi_G)}{d\phi_G} = 0$ containing this term are undefined.

In addition, we check, if the points at the corners of the domain Ω, $(\phi_L,\phi_G) = (0,0), (0,1), (1,0)$, and $(1,1)$ are local energy minima by determining the sign of $\frac{dE(\phi_L,\phi_G)}{d\phi_G}$ and $\frac{dE(\phi_L,\phi_G)}{d\phi_L}$ at these points. They are represented by the green crosses shown in Fig. 5, and the conditions for them to be a local energy minimum are presented in Table I. The derivations $\frac{dE(0,0)}{d\phi_G}$, $\frac{dE(0,1)}{d\phi_G}$, $\frac{dE(1,0)}{d\phi_G}$, and $\frac{dE(1,1)}{d\phi_G}$ are included in Appendix F and depend on S, and therefore, it is dependent on S whether the corner is a local minimum or not. Overall, the set of local energy minima depends on S and all the local energy minima are at the boundary of Ω. The physical understanding on the equilibrium values of ϕ_L and ϕ_G on the boundary of Ω is as follows.

- $\phi_L = 0$: no liquid penetrating into the solid beneath the liquid droplet, we term this state as the micro Cassie–Baxter state for the liquid phase;

TABLE I. Conditions of the sign of $\frac{dE}{d\phi_G}$ and $\frac{dE}{d\phi_L}$ for the existence of local energy minima at the corners $(\phi_L, \phi_G) = (0,0), (0,1), (1,0)$ and $(1, 1)$ of the domain $\{(\phi_L, \phi_G) | 0 \le \phi_L \le 1, 0 \le \phi_G \le 1\}$.

ϕ_L	ϕ_G		
0	0	$\frac{dE(0,0)}{d\phi_G} > 0$	$\frac{dE(0,0)}{d\phi_L} > 0$
0	1	$\frac{dE(0,1)}{d\phi_G} < 0$	$\frac{dE(0,1)}{d\phi_L} > 0$
1	0	$\frac{dE(1,0)}{d\phi_G} > 0$	$\frac{dE(1,0)}{d\phi_L} < 0$
1	1	$\frac{dE(1,1)}{d\phi_G} < 0$	$\frac{dE(1,1)}{d\phi_L} < 0$

- $\phi_L = 1$: no gas penetrating into the solid beneath the liquid droplet, and we term this state as the micro Wenzel state for the liquid phase;
- $0 < \phi_L < 1$: liquid and gas penetrating into the solid beneath the liquid droplet;
- $\phi_G = 0$: no liquid penetrating into the solid under the gas droplet, and we term this state as the micro Cassie–Baxter state for the gas phase;
- $\phi_G = 1$: no gas penetrating into the solid under the gas droplet, and we term this state as the micro Wenzel state for the gas phase; and
- $0 < \phi_G < 1$: liquid and gas penetrating into the solid beneath the gas phase.

Moreover, there is a possible saddle point or maximum, marked by the red cross shown in Fig. 5. This point $\phi_L = \frac{1}{2} - \frac{\Delta p - \Delta\chi}{2\chi}$, $\phi_G = \frac{1}{2} - \frac{\Delta p - \Delta\chi}{2\chi}$ is the solution of the system $\frac{dE}{d\phi_G} = 0, \frac{dE}{d\phi_L} = 0$. The Hessian matrix at this point is

$$\begin{pmatrix} \left[(18\pi V^2)^{\frac{1}{3}} - 2S\right]\ell\chi & 0 \\ 0 & -(18\pi V^2)^{\frac{1}{3}}\ell\chi \end{pmatrix}$$

and has the eigenvalues $\lambda_1 = [(18\pi V^2)^{\frac{1}{3}} - 2S]\ell\chi$ and $\lambda_2 = -(18\pi V^2)^{\frac{1}{3}}\ell\chi < 0$. The type of the critical point and the definiteness of the Hessian matrix dependent on the sign of λ_1 or the value of S is presented in Table II. This point is within the considered domain Ω for $0 < \gamma_1 < \ell\chi$.

TABLE II. Type of the critical point of $\phi_L = \frac{1}{2} - \frac{\Delta p - \Delta\chi}{2\chi}$, $\phi_G = \frac{1}{2} - \frac{\Delta p - \Delta\chi}{2\chi}$ and definiteness of the Hessian matrix dependent of the sign of λ_1 or S.

Sign of λ_1	S	Type of extreme point of $\phi_L = \frac{1}{2} - \frac{\Delta p - \Delta\chi}{2\chi}$, $\phi_G = \frac{1}{2} - \frac{\Delta p - \Delta\chi}{2\chi}$	Type of critical point
Positive	$< \frac{(18\pi V^2)^{\frac{1}{3}}}{2}$	Indefinite	Saddle point
Negative	$> \frac{(18\pi V^2)^{\frac{1}{3}}}{2}$	Indefinite	Maximum
Zero	$= \frac{(18\pi V^2)^{\frac{1}{3}}}{2}$	Negative semidefinite	Not decidable via Hessian matrix

B. Dependence of the energy E and Young's contact angle on the parameter γ_0

In this section, we consider the dependence of E on the parameter γ_0 in the wall energy function Eq. (5). By substituting Eq. (5) into Eq. (16),

$$\begin{aligned} \frac{E(\phi_L, \phi_G)}{\sigma(3V\sqrt{\pi})^{\frac{2}{3}}} &= [2+\mu]^{\frac{1}{3}}[1-\mu]^{\frac{2}{3}} + \frac{\gamma(\phi_G)S}{\sigma(3V\sqrt{\pi})^{\frac{2}{3}}} \\ &= \left(2 + \frac{\rho}{\sigma}\right)^{\frac{1}{3}}\left(1 - \frac{\rho}{\sigma}\right)^{\frac{2}{3}} \\ &\quad + \frac{(\gamma_2\phi_G^2 + \gamma_1\phi_G)S}{\sigma(3V\sqrt{\pi})^{\frac{2}{3}}} + \frac{\gamma_0 S}{\sigma(3V\sqrt{\pi})^{\frac{2}{3}}}, \end{aligned}$$

with $\mu = \frac{a(\phi_L, \phi_G)}{\sigma}$ and $\rho = \gamma_2\phi_G^2 + \gamma_1\phi_G - \gamma_2\phi_L^2 - \gamma_1\phi_L$, we observe, that only the last term depends on γ_0 and this term does not depend on ϕ_L and ϕ_G. Therefore, for different choices of γ_0, a different constant is added to the energy E. Therefore, we will confine to energy maps with $\gamma_0 = 0$, since the plots for different γ_0 will not distinguish from each other apart from an added constant. It should be noted that Young's contact angle θ does not depend on the choice of γ_0, as shown in the following calculation. For brevity, we will not show maps of Young's contact angle for different values of γ_0,

$$\begin{aligned} \cos\theta(\phi_L, \phi_G) &= \frac{a(\phi_L, \phi_G)}{\sigma} \\ &= \frac{\gamma_2\phi_G^2 + \gamma_1\phi_G - \gamma_2\phi_L^2 - \gamma_1\phi_L}{\sigma}. \end{aligned}$$

C. Contact angle hysteresis

The experimental contact angle θ can be in the range of the advancing and receding contact angles $\theta_{rec} < \theta < \theta_{adv}$, depending on the physical conditions. This effect can be observed, for example, by tilting the surface until the drop starts sliding due to the increase in the gravity.[15] The advancing and receding contact angles are quantified by the maximum and the minimum of the equilibrium contact angles. The contact angle hysteresis (CAH) denotes the difference between the maximum (θ_{adv}) and the minimum (θ_{rec}) of the contact angles at the equilibrium state, which is with local minimal energy,

$$\text{CAH} := \theta_{adv} - \theta_{rec}. \tag{20}$$

Contact angle hysteresis can be caused, for example, by heterogeneity, roughness of the substrate, and by deformation or adaption of the substrate by the contact line.[15] In the following sections, we will see that there exist multiple local energy minima by considering non-constant liquid–solid and solid–gas interfacial energies as well as the additional term $\gamma(\phi_G)S$. From Eq. (15), we see that Young's contact angle does not depend on the additional energy contribution, $\gamma(\phi_G)S$ or S. However, the existence of the local energy minima at the possible points depends on S, as described in Sec. II A. Therefore, the set of contact angles and, consequently, also the contact angle hysteresis depends on S.

III. ENERGY LANDSCAPE PLOTS OF A LIQUID DROPLET

In the following, we will see plots for three cases of $(\Delta p - \Delta\chi)/\chi$.

- Case (a): $\chi < \Delta p - \Delta\chi$;
- Case (b): $\chi \geq \Delta p - \Delta\chi$; and
- Case (c): $\chi \gg \Delta p - \Delta\chi$.

For all maps shown in Figs. 6, 10, and 14, we set the following parameters: $V = 1$ and $2\ell\chi/\sigma = 1$. The volume of the droplet has an arbitrary unit, so long as the Bond number is much less than unity and the droplet shape is a spherical cap. On the left side of Figs. 6, 10, and 14, denoted by (i), the energy landscape $E(\phi_L, \phi_G)$ is shown for different values of $S/V^{\frac{2}{3}}$. The first value $S/V^{\frac{2}{3}} = 0$ is included, even though it makes no physical sense, to show the results for the energy formula without the additional term $\gamma(\phi_G)S$ for comparing with the results from other publications, which did not include the additional term.[3] In the middle, the figures indicated by (ii) illustrate the map of Young's contact angle $\theta(\phi_L, \phi_G)$. The additional term, $\gamma(\phi_G)S$ does not affect Young's contact angle, as derived in Eq. (15). So, the maps of Young's contact angle are equivalent for different values of S. The figures only distinguish from each other by the contact angles at the minimum energy state, which are marked by a cross in the maps for Young's contact angle. The right side, denoted with (iii) displays the shape of the droplet at the equilibrium state, that is, by minimal energy with a constant volume V. In addition, Figs. 7, 11, and 15 show the number of local energy minima, dependent of $S/V^{\frac{2}{3}}$; Figs. 8, 12, and 16 show the corresponding Young's contact angles. The points in these plots mark the values shown in Figs. 6, 10, and 14, and the lines are based on by analysis of the energy minima in Sec. II A. In Figs. 9, 13, and 17, the dependence of the contact angle hysteresis on the ratio $S/V^{\frac{2}{3}}$ is shown.

A. Case (a)

In the first case, we assume $\chi < \Delta p - \Delta\chi$ or equivalently $\gamma_1 < 0$. Here, $\frac{\Delta p - \Delta\chi}{\chi} = 2$ and, therefore, $\gamma_1 = 1 - \frac{\Delta p - \Delta\chi}{\chi} = -1$ and

$$\gamma(\phi) = 2\sigma(-\phi^2 - \phi)$$

were chosen. So, the difference between the pressure force and the van der Waals force is greater than the $L - G$ intermolecular force. The energy landscape of $S/V^{\frac{2}{3}} = 0$ decreases from the upper left corner (0, 1) to the lower right corner (1, 0) with a series of diagonal contour lines. This develops to a decrease in the energy landscape of $S/V^{\frac{2}{3}} = 100$ from the lower left corner (0, 0) to the upper right corner (1, 1) with almost horizontal contour lines. The possible saddle point or maximum is outside of the domain Ω, which corresponds to Sec. II A. The map of Young's contact angle is qualitatively the same as the energy map for $S/V^{\frac{2}{3}} = 0$. The number and position of the local energy minima, marked by crosses shown in Figs. 6(a-ii)–6(i-ii), agree with Sec. II A. For the first four values of $S/V^{\frac{2}{3}}$, there is only one local energy minimum at $\phi_L = 1$ and $\phi_G = 0$ in the energy landscape, as shown in Figs. 6(a-ii)–6(d-ii). The contact angle at the energy minimum state is zero. At this equilibrium, no gas penetrates

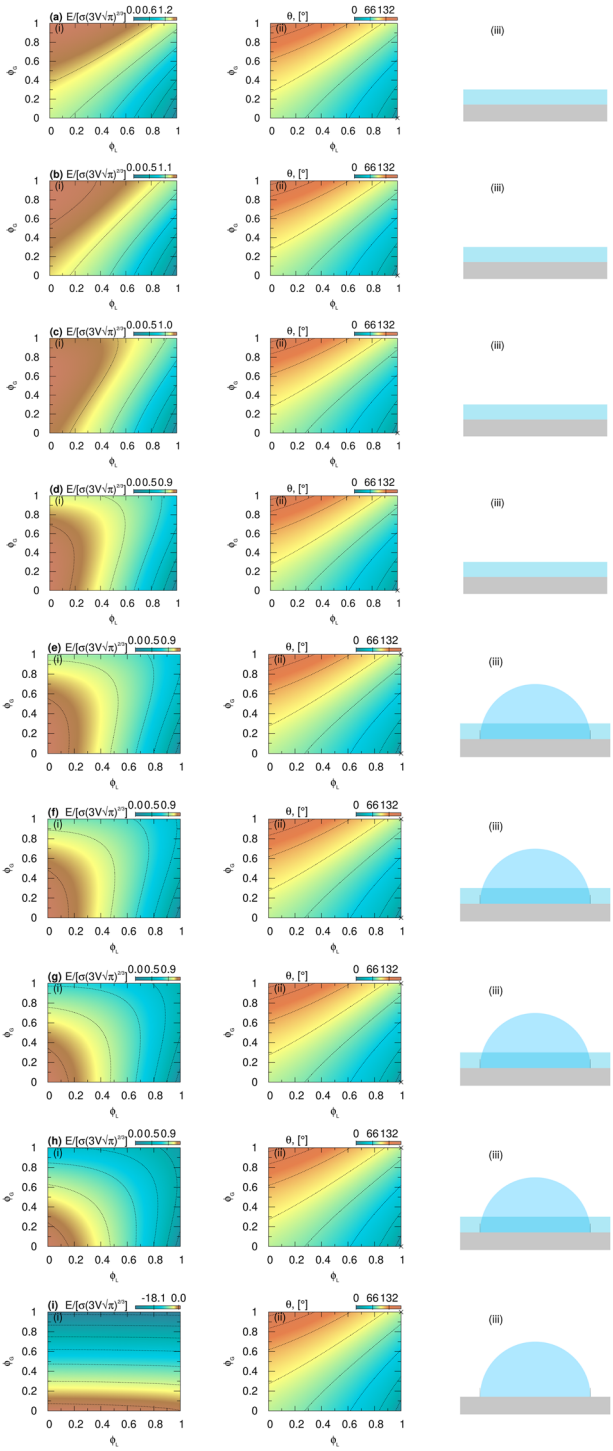

FIG. 6. (i) Energy landscape $E(\phi_L, \phi_G)$, (ii) map of the Young's contact angle, and (iii) shape of the droplet at the equilibrium states with $V = 1$, $2\ell\chi/\sigma = 1$, $\frac{\Delta p - \Delta\chi}{\chi} = 2$ and (a) $S/V^{\frac{2}{3}} = 0$, (b) $S/V^{\frac{2}{3}} = 0.5$, (c) $S/V^{\frac{2}{3}} = 1$, (d) $S/V^{\frac{2}{3}} = 1.7$, (e) $S/V^{\frac{2}{3}} = 1.95$, (f) $S/V^{\frac{2}{3}} = 2.1$, (g) $S/V^{\frac{2}{3}} = 2.5$, (h) $S/V^{\frac{2}{3}} = 3$, and (i) $S/V^{\frac{2}{3}} = 100$.

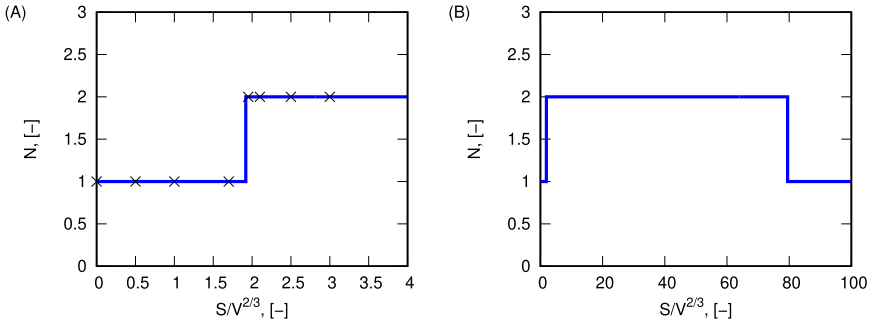

FIG. 7. Number of local energy minima in the domain $\{(\phi_L, \phi_G)|0 \le \phi_L \le 1, 0 \le \phi_G \le 1\}$ depending on $S/V^{\frac{2}{3}}$ for $V = 1$, $2\ell\chi/\sigma = 1$, and $\frac{\Delta p - \Delta\chi}{\chi} = 2$ for different ranges (a) $S/V^{\frac{2}{3}} \in [0, 4]$ with the lines corresponding to the analysis in Sec. II A and the crosses corresponding to the energy minima shown in Fig. 6 and (b) $S/V^{\frac{2}{3}} \in [0, 100]$.

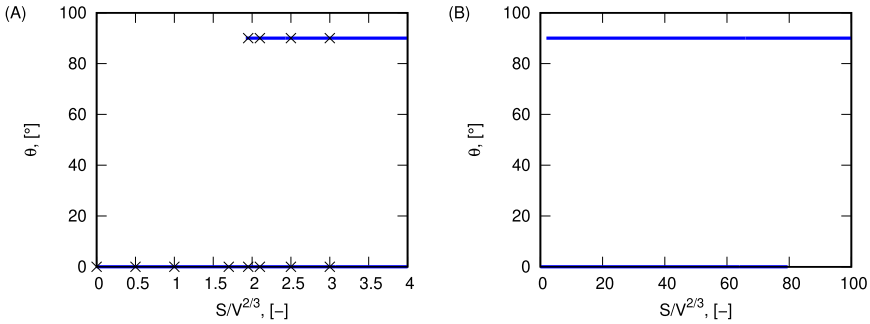

FIG. 8. Young's contact angles θ corresponding to the local energy minima depending on $S/V^{\frac{2}{3}}$ for $V = 1$, $2\ell\chi/\sigma = 1$, and $\frac{\Delta p - \Delta\chi}{\chi} = 2$ for different ranges (a) $S/V^{\frac{2}{3}} \in [0, 4]$ with the lines corresponding to the analysis in Sec. II A and crosses corresponding to the energy minima shown in Fig. 6 and (b) $S/V^{\frac{2}{3}} \in [0, 100]$.

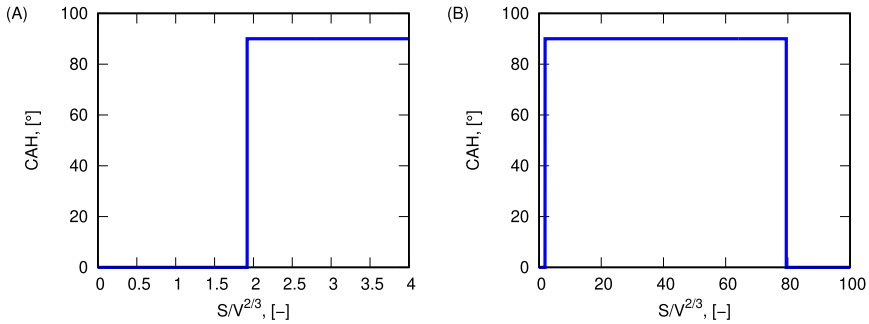

FIG. 9. Contact angle hysteresis depending on $S/V^{\frac{2}{3}}$ for $V = 1$, $2\ell\chi/\sigma = 1$, and $\frac{\Delta p - \Delta\chi}{\chi} = 2$ (a) $S/V^{\frac{2}{3}} \in [0, 4]$ and (b) $S/V^{\frac{2}{3}} \in [0, 100]$.

into the solid under the liquid droplet; no liquid penetrates into the solid at the gas phase.

For the next four values of $S/V^{\frac{2}{3}}$, there is an additional local energy minimum occurring at $\phi_L = 1$ and $\phi_G = 1$ with a contact angle of 90°, while the setup of $S/V^{\frac{2}{3}} = 100$ has only one energy minimum with a contact angle of 90°. No liquid penetrates into the solid under the liquid droplet and the gas phase. The difference between these two possible equilibrium contact angles is large. The number of the local minima N of the energy landscape for different values of S is shown in Fig. 7. Figure 8 shows the contact angles corresponding to the local energy minima depending on $S/V^{\frac{2}{3}}$, therefore, the possible equilibrium states of the droplet. The crosses in Figs. 7(a) and 8(a) represent the number of local energy minima and the corresponding Young's contact angles shown in Fig. 6. They match the line plots in these figures. The contact angle hysteresis is shown in Fig. 9. Figures 7(b), 8(b), and 9(b) show a higher range as Figs. 7(a), 8(a), and 9(a). It can be observed that there is no monotonic increase in the number of energy minima and contact angle hysteresis with

increasing $S/V^{\frac{2}{3}}$. For a large range of $S/V^{\frac{2}{3}} \in (1.919, 79.5)$, there are two local energy minima with different Young's contact angles. These two contact angle hysteresis have a huge difference (of 90°), and consequently, there is a huge contact angle hysteresis in this range. Outside this range, there is only one local energy minimum and, therefore, only one Young's contact angle and no contact angle hysteresis. As a summary for case (a), we have

$$\mathrm{CAH} = \begin{cases} 0^\circ & S/V^{\frac{2}{3}} \le 1.919, \\ 90^\circ & 1.919 < S/V^{\frac{2}{3}} < 79.5, \\ 0^\circ & 79.5 \le S/V^{\frac{2}{3}}. \end{cases}$$

For a contact angle $\theta = 0^\circ$, a liquid film on the solid substrate is shown in Figs. 6(a-iii)–6(h-iii).

B. Case (b)

In the second case, $\chi \ge \Delta p - \Delta\chi$ or equivalently $\gamma_1 \ge 0$ holds. Here, we choose $\frac{\Delta p - \Delta\chi}{\chi} = 0.5$, $\gamma_1 = 1 - \frac{\Delta p - \Delta\chi}{\chi} = 0.5$ and

$$\gamma(\phi) = 2\sigma\left(-\phi^2 + \frac{1}{2}\phi\right).$$

The energy landscape possesses hyperbolic contour lines asymmetric to the $\phi_L = 0.5$ and $\phi_G = 0.5$ axes with maxima at the $\phi_L = 0$ and $\phi_L = 1$ axes and minima at the $\phi_G = 0$ and $\phi_G = 1$ axes for small $S/V^{\frac{2}{3}}$. This can, for example, be observed in Fig. 10(a-i). For large $S/V^{\frac{2}{3}}$, the energy landscape, for example, Fig. 10(h-i), shows one maximum in the lower left quadrant and horizontally stretched elliptical contour lines. For $S < \frac{(18\pi)^{\frac{1}{3}}}{2} \approx 1.919$, the point (0.25, 0.25) is a saddle point [see Figs. 10(a-i)–10(d-i)]; otherwise, it is a maximum [Figs. 10(e-i)–10(i-i)]. The map of Young's contact angle is qualitatively the same as the energy map for $S/V^{\frac{2}{3}} = 0$. The number and position of the local energy minima and the saddle point or maximum, marked by crosses shown in Figs. 10(a-ii)–10(i-ii), agree with Sec. II A. The number of local minima N of the energy landscape for different values of S is shown in Fig. 11 on the left. It is not increasing with increasing $S/V^{\frac{2}{3}}$. There are two peaks at $S/V^{\frac{2}{3}} \in (1.919, 1.9796)$ and $S/V^{\frac{2}{3}} \in (2.441, 2.515)$. These peaks occur due to the transition of the energy landscape from hyperbolic to elliptic. The peaks appear in these ranges because the energy minima of the values of $S/V^{\frac{2}{3}}$ is slightly less than the values of the range and additionally the energy minima of the values slightly higher than the range occur simultaneously. This can be observed in Fig. 12 or in Fig. 10(e-ii) for the first peak and in Fig. 10(g-ii) for the second peak. Figure 11(b) shows the corresponding contact angles depending on $S/V^{\frac{2}{3}}$. Here, the ranges, as described before, are visible. The crosses shown in Figs. 11 and 12 represent the number of local energy minima and the corresponding Young's contact angle shown in Fig. 10. They match the line plots in these figures. The contact angle hysteresis is shown in Fig. 13. In this case, the contact angle hysteresis is not increasing with increasing $S/V^{\frac{2}{3}}$. As a summary for case (b), we have

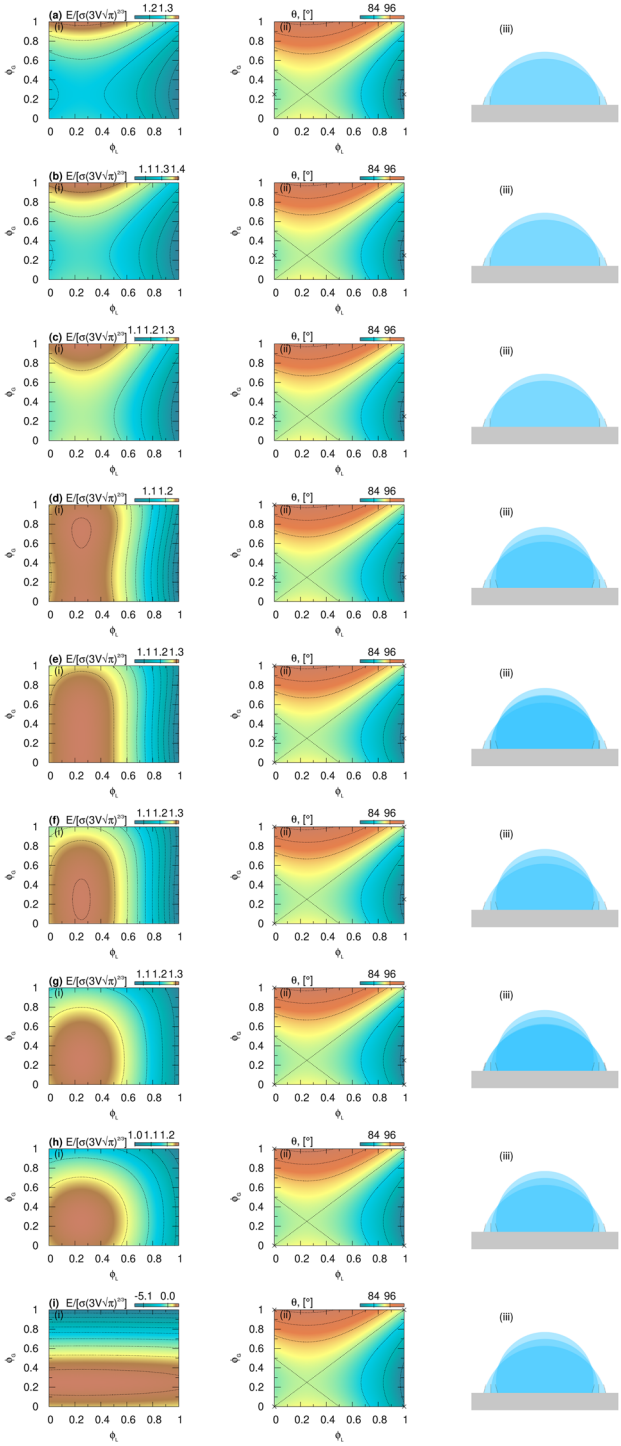

FIG. 10. (i) Energy landscape $E(\phi_L, \phi_G)$, (ii) map of Young's contact angle, and (iii) shape of the droplet at the equilibrium states with $V = 1$, $2\ell\chi/\sigma = 1$, and $\frac{\Delta p - \Delta\chi}{\chi} = 0.5$ and (a) $S/V^{\frac{2}{3}} = 0$, (b) $S/V^{\frac{2}{3}} = 0.5$, (c) $S/V^{\frac{2}{3}} = 1$, (d) $S/V^{\frac{2}{3}} = 1.7$, (e) $S/V^{\frac{2}{3}} = 1.95$, (f) $S/V^{\frac{2}{3}} = 2.1$, (g) $S/V^{\frac{2}{3}} = 2.5$, (h) $S/V^{\frac{2}{3}} = 3$, and (i) $S/V^{\frac{2}{3}} = 100$.

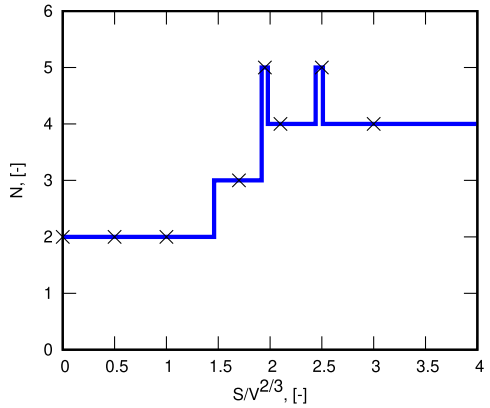

FIG. 11. Number of energy minima in the domain $\{(\phi_L, \phi_G) | 0 \le \phi_L \le 1, 0 \le \phi_G \le 1\}$ depending on $S/V^{\frac{2}{3}}$ for $V = 1$, $2\ell\chi/\sigma = 1$, and $\frac{\Delta p - \Delta\chi}{\chi} = 0.5$ with the lines corresponding to the analysis in Sec. II A and the crosses corresponding to the energy minima shown in Fig. 10.

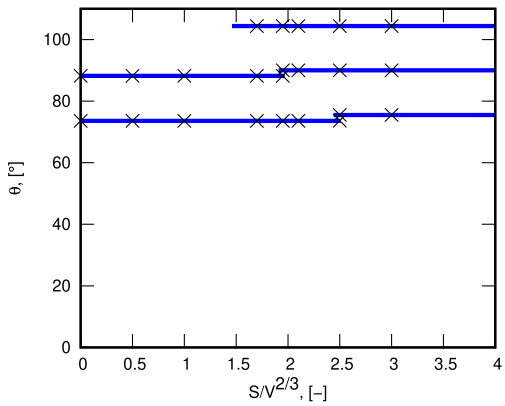

FIG. 12. Young's contact angles θ corresponding to the local energy minima depending on $S/V^{\frac{2}{3}}$ for $V = 1$, $2\ell\chi/\sigma = 1$, and $\frac{\Delta p - \Delta\chi}{\chi} = 0.5$ with the lines corresponding to the analysis in Sec. II A and the crosses corresponding to the energy minima shown in Fig. 10.

$$\mathrm{CAH} = \begin{cases} 14.544^\circ & S/V^{\frac{2}{3}} \le 1.46, \\ 30.812^\circ & 1.46 < S/V^{\frac{2}{3}} < 2.5145, \\ 28.955^\circ & 2.5145 \le S/V^{\frac{2}{3}}. \end{cases}$$

The contact angle hysteresis occurs for every value of $S/V^{\frac{2}{3}}$. There is a range of $S/V^{\frac{2}{3}} \in (1.46, 2.5145)$, in which the contact angle hysteresis is higher than below and above this range.

C. Case (c)

In the third case, $\chi \gg \Delta p - \Delta\chi$ or equivalently $\gamma_1 \gg 0$ holds. Here, we choose $\frac{\Delta p - \Delta\chi}{\chi} = 0$, $\gamma_1 = 1 - \frac{\Delta p - \Delta\chi}{\chi} = 1$ and

$$\gamma(\phi) = 2\sigma(-\phi^2 + \phi).$$

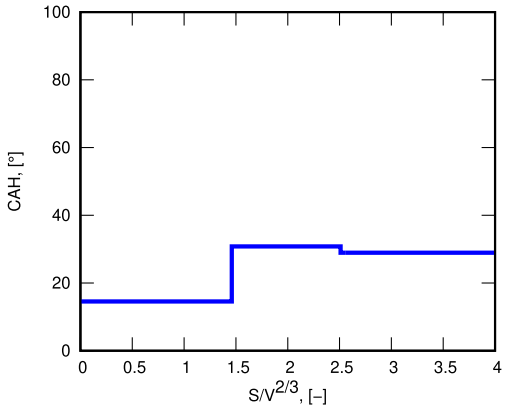

FIG. 13. Contact angle hysteresis depending on $S/V^{\frac{2}{3}}$ for $V = 1$, $2\ell\chi/\sigma = 1$, and $\frac{\Delta p - \Delta\chi}{\chi} = 2$ with the lines corresponding to the analysis in Sec. II A and the crosses corresponding to the energy minima shown in Fig. 10.

The energy landscape of small $S/V^{\frac{2}{3}}$, for example Fig. 14(a-i), has hyperbolic contour lines symmetric to the $\phi_L = 0.5$ axis and the $\phi_G = 0.5$ axis with maxima at the $\phi_L = 0$ axis and the $\phi_L = 1$ axis and minima at the $\phi_G = 0$ axis and the $\phi_G = 1$ axis. In contrast to this, the energy landscape of large $S/V^{\frac{2}{3}}$, as shown in Fig. 14(i-i), has one maximum in the center and elliptical, symmetric and horizontally stretched contour lines. For $S < \frac{(18\pi)^{\frac{1}{3}}}{2} \approx 1.919$, the point (0.5, 0.5) is a saddle point [Figs. 14(a-i)–14(d-i)]; otherwise, it is a maximum [Figs. 14(e-i)–14(i-i)]. The map of Young's contact angle is qualitatively the same as the energy map for $S/V^{\frac{2}{3}} = 0$. The number and position of the local energy minima and the saddle point or maximum, marked by crosses shown in Figs. 14(a-ii)–14(i-ii), agree with Sec. II A. For the first four values of $S/V^{\frac{2}{3}}$, there are two local energy minima at $(\phi_L, \phi_G) = (0, 0.5)$ and $(\phi_L, \phi_G) = (1, 0.5)$, which are shown in Figs. 14(a-ii)–14(d-ii). Both equilibria belong to a contact angle of 82.8°. At the first energy minimum, no liquid penetrates into the solid beneath the liquid droplet and liquid and gas penetrate equally into the solid beneath the gas phase. The second equilibrium behaves as follows: no gas penetrates into the solid beneath the liquid droplet, and liquid and gas penetrate equally into the solid beneath the gas phase. At the next two values of $S/V^{\frac{2}{3}}$, there are additional local energy minima at (0, 1), (1, 0), (0, 0), and (1, 1), as shown in Figs. 14(e-ii) and 14(f-ii). The contact angle of these equilibria is 90°. Here, all combinations of no gas or no liquid penetrating beneath the droplet and no gas or no liquid penetrating beneath the gas phase occur. The last two cases, as shown in Figs. 14(g-ii)–14(i-ii), possess the equilibria, (0, 1), (1, 0), (0, 0), and (1, 1) with the same properties as described before. In this section, the energy landscape and the map of Young's contact angle are symmetric to the $\phi_G = 0.5$ axis and the $\phi_L = 0.5$ axis. The symmetry of the energy landscape and Young's contact angle to the $\phi_G = 0.5$ axis and the $\phi_L = 0.5$ axis occurs due to the symmetry of $\gamma(\phi)$ to 0.5,

$$\begin{aligned} \gamma(\phi) &= 2\sigma(-\phi^2 + \phi) \\ &= 2\sigma\left[\frac{1}{4} - \left(\phi - \frac{1}{2}\right)^2\right]. \end{aligned}$$

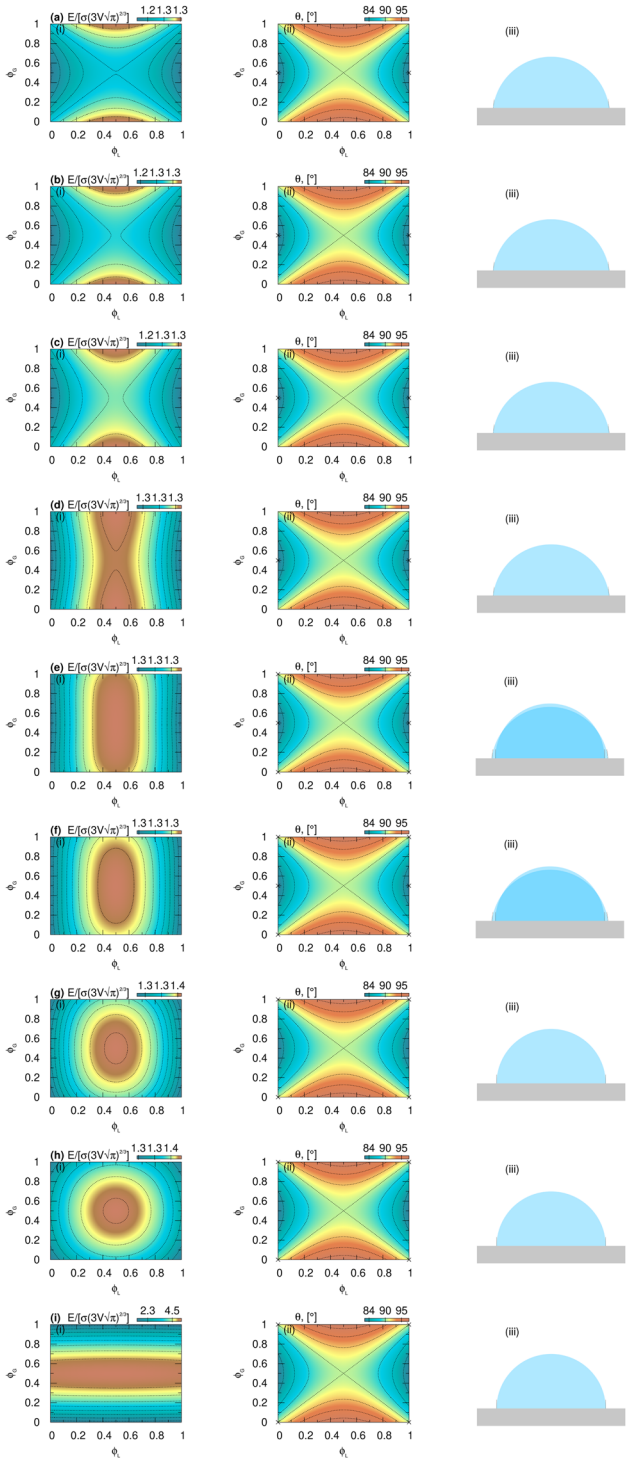

FIG. 14. (i) Energy landscape $E(\phi_L, \phi_G)$, (ii) map of Young's contact angle, and (iii) shape of the droplet at the equilibrium states with $V = 1$, $2\ell\chi/\sigma = 1$, and $\frac{\Delta p - \Delta\chi}{\chi} = 0$ and (a) $S/V^{\frac{2}{3}} = 0$, (b) $S/V^{\frac{2}{3}} = 0.5$, (c) $S/V^{\frac{2}{3}} = 1$, (d) $S/V^{\frac{2}{3}} = 1.7$, (e) $S/V^{\frac{2}{3}} = 1.95$, (f) $S/V^{\frac{2}{3}} = 2.1$, (g) $S/V^{\frac{2}{3}} = 2.5$, (h) $S/V^{\frac{2}{3}} = 3$, and (i) $S/V^{\frac{2}{3}} = 100$.

Therefore, the two contact angles at the local energy minimum at the same value of ϕ_G have the same contact angle, and the local energy minima are also symmetric to the $\phi_G = 0.5$ axis and the $\phi_L = 0.5$ axis. The number of local minima of the energy landscape N for different values of $S/V^{\frac{2}{3}}$ is shown in Fig. 15. It is not increasing with increasing $S/V^{\frac{2}{3}}$ since there is a peak at $S/V^{\frac{2}{3}} \in (1.919, 2.168)$. This peak occurs due to the transition of the energy landscape from hyperbolic to elliptic. There is a range of $S/V^{\frac{2}{3}}$, where the energy minimum of the values of $S/V^{\frac{2}{3}}$ is slightly less than the values of the range, and additionally, the energy minimum of the values slightly higher than the range occur simultaneously, as shown in Figs. 14(e-ii) and 14(f-ii) or in Fig. 15 for $S/V^{\frac{2}{3}} \in (1.919, 2.16)$. For $S/V^{\frac{2}{3}} \in (0, 2.16)$, there are four and for $S/V^{\frac{2}{3}} \in (2.16, \infty)$, six local energy minima. Figure 17 shows that contact angle hysteresis occurs only at this small range of $S/V^{\frac{2}{3}} \in (1.919, 2.16)$. Outside of this range, there is no contact angle hysteresis. Figure 15 shows the corresponding contact angles depending on $S/V^{\frac{2}{3}}$, which are comparatively high (close to 90° or 90°), as shown in Fig. 16. The crosses shown in Figs. 15 and 16 represent the number of local energy minima and the corresponding Young's contact angle shown in Fig. 14. They match the line plots in these figures. In this case, the contact angle hysteresis is not increasing with increasing $S/V^{\frac{2}{3}}$. As a summary for case (c), we have

$$\mathrm{CAH} = \begin{cases} 0^\circ & S/V^{\frac{2}{3}} \le 1.919, \\ 7.18^\circ & 1.919 < S/V^{\frac{2}{3}} < 2.1679, \\ 0^\circ & 2.1679 \le S/V^{\frac{2}{3}}. \end{cases}$$

D. Comparison of cases (a), (b), and (c)

In Secs. III A–III C, we used different values of $\frac{\Delta p - \Delta\chi}{\chi}$, which leads to different values of γ_1 with (a) $\chi < \Delta p - \Delta\chi, \gamma_1 < 0$, (b) $\chi \ge \Delta p - \Delta\chi, \gamma_1 \ge 0$, and (c) $\chi \gg \Delta p - \Delta\chi, \gamma_1 \gg 0$.

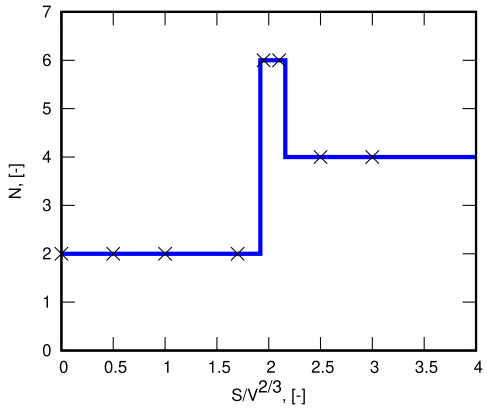

FIG. 15. Number of energy minima in the domain $\{(\phi_L, \phi_G) | 0 \le \phi_L \le 1, 0 \le \phi_G \le 1\}$ depending on $S/V^{\frac{2}{3}}$ for $V = 1$, $2\ell\chi/\sigma = 1$, and $\frac{\Delta p - \Delta\chi}{\chi} = 0$ with the lines corresponding to the analysis in Sec. II A and the crosses corresponding to the energy minima shown in Fig. 14.

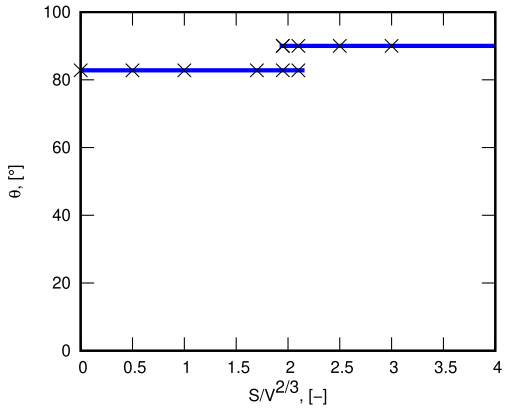

FIG. 16. Young's contact angles θ corresponding to the local energy minima depending on $S/V^{\frac{2}{3}}$ for $V = 1$, $2\ell\chi/\sigma = 1$, and $\frac{\Delta p - \Delta\chi}{\chi} = 0$ with the lines corresponding to the analysis in Sec. II A and the crosses corresponding to the energy minima shown in Fig. 14.

All in all, we obtain different energy maps, maps of the contact Young's contact angle, and behavior of the energy minima. For all three cases, the energy landscape is changing with different values of $S/V^{\frac{2}{3}}$. The number of local energy minima is not increasing with an increasing value of $S/V^{\frac{2}{3}}$.

For cases (a) and (b), the energy landscapes are asymmetric, whereas for case (c), they are symmetric with respect to $\phi_L = 0.5$ and $\phi_G = 0.5$. In case (a), there is no extreme value at the interior of $\{(\phi_L, \phi_G) | 0 \le \phi_L \le 1, 0 \le \phi_G \le 1\}$, whereas at case (b) and (c), there is a saddle point for $S < \frac{(18\pi)^{\frac{1}{3}}}{2}$ and a maximum for $S > \frac{(18\pi)^{\frac{1}{3}}}{2}$. There is a lower number of local energy minima, a high contact angle hysteresis, and a large range of $S/V^{\frac{2}{3}}$, where the contact angle hysteresis occurs, for case (a) compared to case (c). For cases (b) and (c), there are transition ranges, where the minima of values of $S/V^{\frac{2}{3}}$ lower and higher than the range appear simultaneously. In addition for cases (b) and (c), the energy landscape transforms from hyperbolic to elliptic for higher values of $S/V^{\frac{2}{3}}$. In case (b), there occurs contact angle hysteresis for all values of $S/V^{\frac{2}{3}}$. There are high Young's contact angles (close to 90°) and only a small range of $S/V^{\frac{2}{3}}$, in which contact angle hysteresis occurs, for case (c).

IV. ENERGY OF A GAS BUBBLE INCLUDING AN ADDITIONAL TERM

The formulas for the energy and the contact angle of the liquid droplet are

$$\frac{E(\phi_L, \phi_G)}{\sigma(3V\sqrt{\pi})^{\frac{2}{3}}} = \left[2 + \frac{\zeta_1}{\sigma}\right]^{\frac{1}{3}} \left[1 - \frac{\zeta_1}{\sigma}\right]^{\frac{2}{3}} + \frac{\gamma(\phi_G)S}{\sigma(3V\sqrt{\pi})^{\frac{2}{3}}}, \tag{21}$$

$$\cos\theta(\phi_L, \phi_G) = \frac{\gamma(\phi_G) - \gamma(\phi_L)}{\sigma}, \tag{22}$$

with $\zeta_1 = \gamma(\phi_G) - \gamma(\phi_L)$. In this section, we will consider the case of a gas bubble in a liquid phase on a solid substrate as shown in Fig. 2.

Here, we use $a = \gamma(\phi_L) - \gamma(\phi_G)$ and the additional term $\gamma(\phi_L)S$. With a similar approach as in Sec. II, we can derive the energy and the contact angle of the gas bubble as

$$\frac{E(\phi_L, \phi_G)}{\sigma(3V\sqrt{\pi})^{\frac{2}{3}}} = \left[2 + \frac{\zeta_2}{\sigma}\right]^{\frac{1}{3}} \left[1 - \frac{\zeta_2}{\sigma}\right]^{\frac{2}{3}} + \frac{\gamma(\phi_L)S}{\sigma(3V\sqrt{\pi})^{\frac{2}{3}}}, \tag{23}$$

$$\cos(\pi - \theta(\phi_L, \phi_G)) = \frac{\gamma(\phi_L) - \gamma(\phi_G)}{\sigma}, \tag{24}$$

with $\zeta_2 = \gamma(\phi_L) - \gamma(\phi_G)$. By replacing ϕ_L by ϕ_G and ϕ_G by ϕ_L in Eqs. (23) and (24), Eq. (23) gets to Eq. (21) and Eq. (24) gets to Eq. (22). We obtain the energy landscape for the gas bubble by mirroring the energy landscape of the liquid droplet along the bisector axis. This also holds for the map of Young's contact angle θ of the liquid droplet and the map of $\pi - \theta$ of the gas bubble.

V. COMPARISON OF THE RESULTS WITH THE LITERATURE

Tadmor[16] used a constant $L - S$ and $S - G$ surface tension. In Tadmor's work, there is no contact angle hysteresis for a Young's contact angle equal to 90°. This observation is somehow consistent with the trend of the experimental values of Lam *et al.*[17] They used a "systematic series of hydrocarbon chains"[16] to study the behavior of advancing and receding contact angles and "observed that the advancing and receding contact angles become very close when extrapolated to 90°."[16] For non-constant surface tensions of $\gamma(\phi_L)$ and $\gamma(\phi_G)$, as investigated in this work, this is not true. For example, in case (c) in Sec. III C shown in Fig. 17, there exists a contact angle hysteresis of 7.18° for some values of $S/V^{\frac{2}{3}}$, whereby Young's contact angle is 90° or close to 90°. Our results provide a supplement to Tadmor's work[16] for the case with non-constant surface tensions and with the additional energy contribution, $\gamma(\phi_G)S$.

The results, the energy landscapes, and maps of Young's contact angle of Wang and Nestler[3] match with the plots shown in Figs. 6(a), 10(a), and 14(a) for $S/V^{\frac{2}{3}} = 0$.

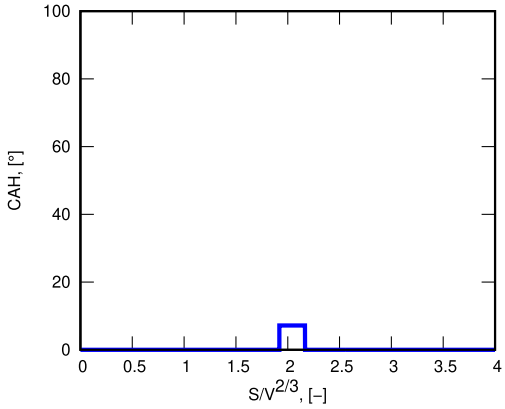

FIG. 17. Contact angle hysteresis depending on $S/V^{\frac{2}{3}}$ for $V = 1$, $2\ell\chi/\sigma = 1$, and $\frac{\Delta p - \Delta\chi}{\chi} = 0$.

VI. CONCLUSION

We have considered the wetting phenomena for a liquid droplet on a solid surface in a gas phase and a gas bubble on a solid surface in a liquid phase. The latter case uses a similar approach as the former one. Our consideration involved roughness on the microscopic scale, where the liquid and the gas species penetrate into the solid phase. In the present calculation, we used a non-constant surface tension of the liquid–solid interface $\gamma(\phi_L)$ and the solid–gas interface, $\gamma(\phi_G)$ with $\gamma(\phi) = \gamma_2\phi^2 + \gamma_1\phi + \gamma_0$, and included an additional energy contribution, $S\gamma(\phi_G)$, in contrast to previous researches with constant fluid–solid interfacial tensions.[1] We analyzed the number of energy minima and the general differences between the plots of the energy landscape, the corresponding Young's contact angle, and the contact angle hysteresis for different choices of γ_1 and the surface of the solid substrate S. For the second and third cases of the considered values of γ_1, there is no monotonic decrease or increase discernible for increasing $S/V^{\frac{2}{3}}$ for the number of the local energy minima and the contact angle hysteresis, since there is a range of $S/V^{\frac{2}{3}}$ in which the energy minima of the values lower than the range and of the values higher than the range occur simultaneously. For the first considered case, there is also no monotonic increase in the number of energy minima and the contact angle hysteresis with an increasing value of $S/V^{\frac{2}{3}}$. Different values of γ_0 add a constant term to the energy, which is independent of ϕ_L and ϕ_G, and do not change the Young's contact angle. In conclusion, the inclusion of the additional term significantly impacts the energy landscape, the number and position of the local energy minima, and the contact angle hysteresis, while it does not affect Young's contact angle.

VII. OUTLOOK

In these considerations, one could also include the macroscopic roughness of the solid substrate using the Wenzel equation or a solid substrate consisting of multiple materials using the Cassie–Baxter equation.[1]

For the gas bubble, the gravity effect of the water phase on the gas bubble could also be included. This would lead to a non-closed form of the energy compared to Eq. (11). In addition, it could be investigated which contact angle the gas bubble forms compared to the liquid droplet under equivalent conditions.

In the current work, we have neglected the contribution of the pressure energy to the wall free energy. An additional term containing, for example, the Derjaguin disjoining pressure,[18] could also be included in the wall free energy. It is expected that the pressure associated energy affects the energy minimization and thus the contact angle hysteresis. The present work focuses on the case of Bond number much less than unity. When the Bond number is close to or greater than 1, the bulk free energy, including the excess pressure energy, has to be considered in the energy minimization process. This complex scenario will be addressed in a forthcoming work.

ACKNOWLEDGMENTS

F.A. acknowledges the Gottfried-Wilhelm Leibniz prize Grant No. NE 822/31-1 of the German Research Foundation (DFG) for funding this research. F.W. is grateful to the VirtMat project P09 of the Helmholtz Association (MSE-programme Grant No. 43.31.01).

AUTHOR DECLARATIONS

Conflict of Interest

The authors have no conflicts to disclose.

Author Contributions

Franziska Aurbach: Formal analysis (equal); Investigation (lead); Methodology (equal); Validation (equal); Visualization (equal); Writing – original draft (lead). **Fei Wang**: Conceptualization (lead); Methodology (equal); Supervision (equal); Writing – review & editing (equal). **Britta Nestler**: Funding acquisition (lead); Project administration (lead); Writing – review & editing (equal).

DATA AVAILABILITY

Data sharing is not applicable to this article as no new data were created or analyzed in this study.

APPENDIX A: VOLUME OF THE LIQUID DROPLET

In the first step, we show $\delta = \theta$ from Fig. 18, so we can use θ instead of δ as the integration limit in the following calculations. We can conclude from $\theta + \alpha + \beta = 180°$, from the sum of angles of a triangle $\alpha + \delta + 90° = 180°$ and from $\beta = 90°$ that $\theta = \delta$ holds.

In this appendix, we will derive the formula of the volume of the liquid droplet V in Eq. (1). From Fig. 20, it can be concluded

$$\begin{aligned} \frac{R-h}{R} &= \cos\theta, \\ R - h &= R\cos\theta, \\ h &= R(1-\cos\theta). \end{aligned} \tag{A1}$$

In addition, we can see from Fig. 21,

$$\begin{aligned} f(x)^2 + (x-R)^2 &= R^2, \\ f(x) &= \sqrt{R^2 - (x-R)^2} = \sqrt{2Rx - x^2}. \end{aligned} \tag{A2}$$

By considering the previous equation, we can calculate the volume of the droplet as a spherical cap using solid of revolution as in Fig. 21,

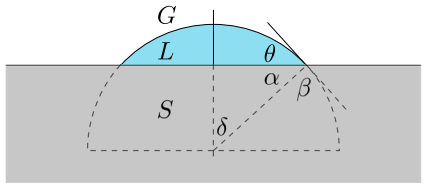

FIG. 18. Illustration of the angles θ, α, β and δ for the proof of $\delta = \theta$ with the liquid droplet L represented by the blue area, the solid substrate S by the gray area, and the gas phase G by the white area.

$$V = \pi \int_0^h f(x)^2 dx = \pi \int_0^h 2Rx - x^2 dx = \pi \left[Rx^2 - \frac{1}{3}x^3 \right]_0^h$$
$$= \pi \left(Rh^2 - \frac{1}{3}h^3 \right) = \frac{\pi}{3}h^2(3R - h)$$
$$= \frac{\pi}{3}R^2(1 - \cos\theta)^2(3R - R + R\cos\theta)$$
$$= \frac{\pi}{3}R^3(1 - \cos\theta)^2(2 + \cos\theta). \quad \text{(A3)}$$

APPENDIX B: SURFACE AREA OF THE LIQUID–AIR INTERFACE

In this section, we will calculate the surface of the liquid–air interface S_d in Eq. (3). The integration values in the spherical coordinate system are shown in Fig. 19,

$$S_d = \int_{S_d} dA = \int_{\tilde{\theta}=0}^{\theta} \int_{\varphi=0}^{2\pi} R^2 \sin\tilde{\theta} d\varphi d\tilde{\theta}$$
$$= R^2 \int_{\tilde{\theta}=0}^{\theta} \sin\tilde{\theta} [\varphi]_0^{2\pi} d\tilde{\theta}$$
$$= 2\pi R^2 \int_{\tilde{\theta}=0}^{\theta} \sin\tilde{\theta} d\tilde{\theta}$$
$$= 2\pi R^2 [-\cos\tilde{\theta}]_0^{\theta}$$
$$= 2\pi R^2 [-\cos\theta + \cos(0)]$$
$$= 2\pi R^2 (1 - \cos\theta).$$

APPENDIX C: PROOF FOR EQ. (13)

In the following, we will prove the first line, which is used in the transformation of Eq. (12) to Eq. (13),

$$\frac{2\sigma - a(1 + \cos\theta)}{(1 - \cos\theta)^{\frac{1}{3}}} = \frac{2\sigma - 2\sigma\cos\theta - (\sin\theta)^2 a}{(1 - \cos\theta)^{\frac{4}{3}}},$$
$$[2\sigma - a(1 + \cos\theta)](1 - \cos\theta) = 2\sigma - 2\sigma\cos\theta - (\sin\theta)^2 a,$$
$$a = a[(\sin\theta)^2 + (\cos\theta)^2]a = a.$$

APPENDIX D: DERIVATIVE OF *E* CONCERNING THE CONTACT ANGLE

In this section, we calculate the derivative of E concerning θ as in Eq. (14). In the following, we will use E instead of $E(\phi_L, \phi_G)$,

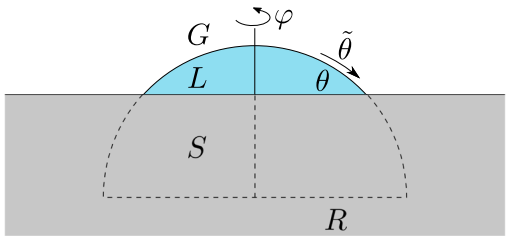

FIG. 19. Illustration of the integration values φ and θ' in the spherical coordinate system with radius R used in Appendix B with the liquid droplet L with the contact angle θ represented by the blue area, the solid substrate S by the gray area, and the gas phase G by the white area.

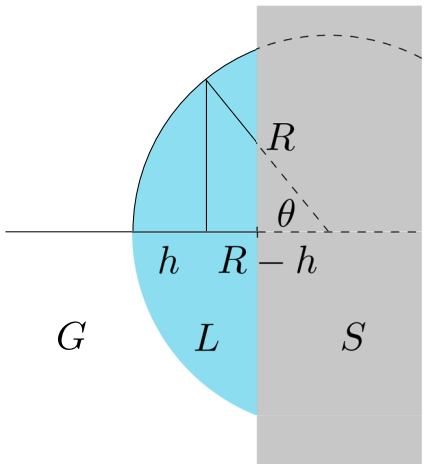

FIG. 20. Illustration of h for the derivation of Eq. (A1) with the side view of the liquid droplet L represented by the blue area, the solid substrate S by the gray area, and the gas phase G by the white area.

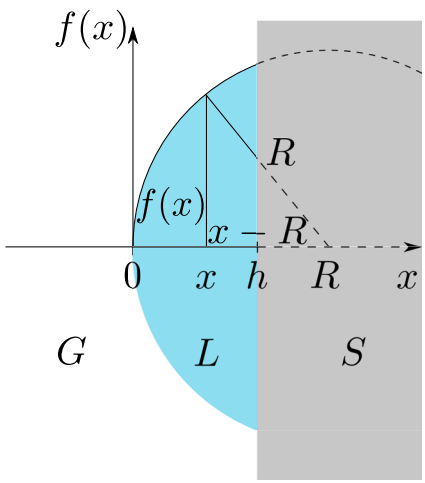

FIG. 21. Illustration of x, $f(x)$, and h for the derivation of Eq. (A2) and the volume of the droplet Eq. (A3) with the side view of the liquid droplet L represented by the blue area, the solid substrate S by the gray area, and the gas phase G by the white area.

$\xi = 1 - \cos\theta$, $\eta = 2 + \cos\theta$, $\iota = 1 + \cos\theta$, $\varepsilon = \sin\theta$, and $w = -4\sigma - 2\sigma\cos\theta + 4\sigma - 4\sigma\cos\theta + 6a$,

$$E = \left(\frac{9V^2\pi}{\xi\eta^2} \right)^{\frac{1}{3}} [2\sigma - a(1 + \cos\theta)] + \sigma(\phi_G)S$$
$$= (9V^2\pi)^{\frac{1}{3}} \frac{2\sigma - a(1 + \cos\theta)}{\xi^{\frac{1}{3}}\eta^{\frac{2}{3}}} + \sigma(\phi_G)S,$$
$$\frac{dE}{d\theta} = (9V^2\pi)^{\frac{1}{3}} \left[\frac{\left(\xi^{\frac{1}{3}}\eta^{\frac{2}{3}}a\varepsilon\right)(2\sigma - a\iota)\left(\frac{1}{3}\xi^{-\frac{2}{3}}\varepsilon\eta^{\frac{1}{3}}\xi^{\frac{1}{3}} \frac{2}{3}\varepsilon\right)}{\xi^{\frac{2}{3}}\eta^{\frac{4}{3}}} \right]$$

$$= (9V^2\pi)^{\frac{1}{3}}\left[\frac{a\varepsilon}{\xi^{\frac{1}{3}}\eta^{\frac{2}{3}}} - \frac{(2\sigma - a\iota)\varepsilon}{3\xi^{\frac{4}{3}}\eta^{\frac{2}{3}}} + \frac{2(2\sigma - a\iota)\varepsilon}{3\xi^{\frac{1}{3}}\eta^{\frac{5}{3}}}\right]$$

$$= (9V^2\pi)^{\frac{1}{3}}\varepsilon\frac{3a\xi\eta - (2\sigma - a\iota)\eta + 2(2\sigma - a\iota)\xi}{3\xi^{\frac{4}{3}}\eta^{\frac{5}{3}}}$$

$$= \frac{(9V^2\pi)^{\frac{1}{3}}\varepsilon}{3\xi^{\frac{4}{3}}\eta^{\frac{5}{3}}}(-2\sigma\eta + 4\sigma\xi + 3a\xi\eta + a\iota\eta - 2a\iota\xi)$$

$$= \frac{(9V^2\pi)^{\frac{1}{3}}\sin\theta w}{3(1-\cos\theta)^{\frac{4}{3}}(2+\cos\theta)^{\frac{5}{3}}}$$

$$= \frac{(9V^2\pi)^{\frac{1}{3}}\sin\theta(-6\cos\theta + 6a)}{3(1-\cos\theta)^{\frac{4}{3}}(2+\cos\theta)^{\frac{5}{3}}}$$

$$= \left[\frac{9V^2\pi}{(1-\cos\theta)^4(2+\cos\theta)^5}\right]^{\frac{1}{3}}2(a - \sigma\cos\theta)\sin\theta.$$

APPENDIX E: DERIVATION OF EQ. (16)

In the following, we will derive Eq. (16). In this section, we will write a instead of $a(\phi_L, \phi_G)$

$$E = \left[\frac{9\pi V^2}{\left(1-\frac{a}{\sigma}\right)\left(2+\frac{a}{\sigma}\right)^2}\right]^{\frac{1}{3}}\left[2\sigma - a\left(1+\frac{a}{\sigma}\right)\right] + \gamma(\phi_G)S$$

$$\frac{E}{\sigma(3V\sqrt{\pi})^{\frac{2}{3}}} = \frac{2 - \frac{a}{\sigma} - \frac{a^2}{\sigma^2}}{\left[1-\frac{a}{\sigma}\right]^{\frac{1}{3}}\left[2+\frac{a}{\sigma}\right]^{\frac{2}{3}}} + \frac{\gamma(\phi_G)S}{\sigma(3V\sqrt{\pi})^{\frac{2}{3}}}.$$

With $2 - \frac{a}{\sigma} - \frac{a^2}{\sigma^2} = \left[1-\frac{a}{\sigma}\right]\left[2+\frac{a}{\sigma}\right]$, we can transform the equation as follows:

$$\begin{aligned}\frac{E}{\sigma(3V\sqrt{\pi})^{\frac{2}{3}}} &= \frac{\left[1-\frac{a}{\sigma}\right]\left[2+\frac{a}{\sigma}\right]}{\left[1-\frac{a}{\sigma}\right]^{\frac{1}{3}}\left[2+\frac{a}{\sigma}\right]^{\frac{2}{3}}} + \frac{\gamma(\phi_G)S}{\sigma(3V\sqrt{\pi})^{\frac{2}{3}}},\\ \frac{E}{\sigma(3V\sqrt{\pi})^{\frac{2}{3}}} &= \left[2+\frac{a}{\sigma}\right]^{\frac{1}{3}}\left[1-\frac{a}{\sigma}\right]^{\frac{2}{3}} + \frac{\gamma(\phi_G)S}{\sigma(3V\sqrt{\pi})^{\frac{2}{3}}}.\end{aligned} \tag{E1}$$

APPENDIX F: DERIVATIVES OF E CONCERNING THE VOLUME FRACTIONS

In the following, the derivatives $\frac{dE(\phi_L,\phi_G)}{d\phi_L}$ and $\frac{dE(\phi_L,\phi_G)}{d\phi_G}$ at the corner points $(0,0),(1,0),(0,1)$ and $(1,1)$ of the domain $\{(\phi_L,\phi_G)|0 \le \phi_L \le 1, 0 \le \phi_G \le 1\}$ are evaluated to identify the local energy minima in Sec. II A. With the usage of $\eta = (\chi\varphi_G + \chi\varphi_L - \chi - \Delta\chi + \Delta p)$, $\bar{\omega} = (\varphi_G - \varphi_L)\eta\ell$, $j = [\bar{\omega} + \sigma]^{\frac{1}{3}}[-\bar{\omega} + 2\sigma]^{\frac{2}{3}}$, $\nu = (\Delta\chi - \Delta p)\ell$, and $m = \nu\ell + \sigma$, we obtain

$$\frac{dE}{d\phi_L} = \frac{3^{\frac{2}{3}}(-\bar{\omega}+\sigma)\pi^{\frac{1}{3}}V^{\frac{2}{3}}[(-2\varphi_L+1)\chi\nu]}{(\bar{\omega}+\sigma)^{\frac{1}{3}}(-\bar{\omega}+2\sigma)^{\frac{2}{3}}},$$

$$\frac{dE}{d\phi_G} = \frac{\left[jS - (3V)^{\frac{2}{3}}(-\bar{\omega}+\sigma)\pi^{\frac{1}{3}}\right][(-2\varphi_G+1)\chi\nu]}{j},$$

$$\frac{dE(0,0)}{d\phi_G} = \frac{2^{\frac{1}{3}}\ell\left(-3^{\frac{2}{3}}\pi^{\frac{1}{3}}V^{\frac{2}{3}} + 2^{\frac{2}{3}}S\right)(\chi - \Delta p + \Delta\chi)}{2},$$

$$\frac{dE(0,0)}{d\phi_L} = \frac{\pi^{\frac{1}{3}}3^{\frac{2}{3}}V^{\frac{2}{3}}\ell(\chi - \Delta p + \Delta\chi)2^{\frac{1}{3}}}{2},$$

$$\frac{dE(0,1)}{d\phi_G} = \frac{\left[(-\nu+\sigma)^{\frac{1}{3}}(\nu+2\sigma)^{\frac{2}{3}}S - 3^{\frac{2}{3}}m\pi^{\frac{1}{3}}V^{\frac{2}{3}}\right](-\chi\ell+\nu)}{(\nu+2\sigma)^{\frac{2}{3}}(-\nu\ell+\sigma)^{\frac{1}{3}}},$$

$$\frac{dE(0,1)}{d\phi_L} = \frac{V^{\frac{2}{3}}[(-\Delta p + \Delta\chi)\ell + \sigma]\ell\,\pi^{\frac{1}{3}}(\chi - \Delta p + \Delta\chi)3^{\frac{2}{3}}}{[(\Delta p - \Delta\chi)\ell + \sigma]^{\frac{1}{3}}[(-\Delta p + \Delta\chi)\ell + 2\sigma]^{\frac{2}{3}}},$$

$$\frac{dE(1,0)}{d\phi_G} = \frac{\left[(-\nu+2\sigma)^{\frac{2}{3}}m^{\frac{1}{3}}S + V^{\frac{2}{3}}\pi^{\frac{1}{3}}3^{\frac{2}{3}}(\nu-\sigma)\right]\chi\nu}{(-\nu+\sigma)^{\frac{1}{3}}(\nu+2\sigma)^{\frac{2}{3}}},$$

$$\frac{dE(1,0)}{d\phi_L} = -\frac{V^{\frac{2}{3}}(-\nu\ell-\sigma)\ell\,\pi^{\frac{1}{3}}(-\chi-\nu)3^{\frac{2}{3}}}{[(\Delta p - \Delta\chi)\ell + 2\sigma]^{\frac{2}{3}}[(-\Delta p + \Delta\chi)\ell + \sigma]^{\frac{1}{3}}},$$

$$\frac{dE(1,1)}{d\phi_G} = -\frac{2^{\frac{1}{3}}\ell\left(-3^{\frac{2}{3}}\pi^{\frac{1}{3}}V^{\frac{2}{3}} + 2^{\frac{2}{3}}S\right)(\chi - \Delta\chi + \Delta p)}{2},$$

$$\frac{dE(1,1)}{d\phi_L} = -\frac{\pi^{\frac{1}{3}}3^{\frac{2}{3}}V^{\frac{2}{3}}\ell(\chi - \Delta\chi + \Delta p)2^{\frac{1}{3}}}{2}.$$

REFERENCES

[1] G. Whyman, E. Bormashenko, and T. Stein, "The rigorous derivation of Young, Cassie–Baxter and Wenzel equations and the analysis of the contact angle hysteresis phenomenon," Chem. Phys. Lett. **450**(4–6), 355–359 (2008).

[2] F. Wang, Y. Wu, and B. Nestler, "Wetting effect on patterned substrates," Adv. Mater. **35**(25), 2210745 (2023).

[3] F. Wang and B. Nestler, "Wetting and contact-angle hysteresis: Density asymmetry and van der Waals force," Phys. Rev. Lett. **132**(12), 126202 (2024).

[4] T. Young, "III. An essay on the cohesion of fluids," Philos. Trans. R. Soc. London **95**, 65–87 (1805).

[5] E. Bormashenko, "Young, Boruvka–Neumann, Wenzel and Cassie–Baxter equations as the transversality conditions for the variational problem of wetting," Colloids Surf., A **345**(1–3), 163–165 (2009).

[6] P. G. de Gennes, "Wetting: Statics and dynamics," Rev. Mod. Phys. **57**(3), 827 (1985).

[7] J. W. Cahn, "Critical point wetting," J. Chem. Phys. **66**(8), 3667–3672 (1977).

[8] H. Zhang, H. Zhang, F. Wang, and B. Nestler, "Wetting effect induced depletion and adsorption layers: Diffuse interface perspective," ChemPhysChem **25**(14), e202400086 (2024).

[9] F. Wang, H. Zhang, Y. Wu, and B. Nestler, "A thermodynamically consistent diffuse interface model for the wetting phenomenon of miscible and immiscible ternary fluids," J. Fluid Mech. **970**, A17 (2023).

[10] P. Yue, "Thermodynamically consistent phase-field modelling of contact angle hysteresis," J. Fluid Mech. **899**, A15 (2020).

[11] P. Yue, C. Zhou, and J. J. Feng, "Sharp-interface limit of the Cahn–Hilliard model for moving contact lines," J. Fluid Mech. **645**, 279–294 (2010).

[12] A. Carlson, G. Bellani, and G. Amberg, "Universality in dynamic wetting dominated by contact-line friction," Phys. Rev. E **85**(4), 045302 (2012).

[13] F. Wang and B. Nestler, "Wetting transition and phase separation on flat substrates and in porous structures," J. Chem. Phys. **154**(9), 094704 (2021).

[14] J. J. Huang, C. Shu, J. J. Feng, and Y. T. Chew, "A phase-field-based hybrid lattice-Boltzmann finite-volume method and its application to simulate droplet motion under electrowetting control," J. Adhes. Sci. Technol. **26**(12–17), 1825–1851 (2012).

[15] H.-J. Butt, J. Liu, K. Koynov, B. Straub, C. Hinduja, I. Roismann, R. Berger, X. Li, D. Vollmer, W. Steffen, and M. Kappl, "Contact angle hysteresis," Curr. Opin. Colloid Interface Sci. **59**, 101574 (2022).

[16] R. Tadmor, "Line energy and the relation between advancing, receding, and young contact angles," Langmuir **20**(18), 7659–7664 (2004).

[17] C. N. C. Lam, R. Wu, D. Li, M. L. Hair, and A. W. Neumann, "Study of the advancing and receding contact angles: Liquid sorption as a cause of contact angle hysteresis," Adv. Colloid Interface Sci. **96**(1–3), 169–191 (2002).

[18] V. M. Starov and M. G. Velarde, "Surface forces and wetting phenomena," J. Phys.: Condens. Matter **21**(46), 464121 (2009).